JOC The Journal of Organic Chemistry

pubs.acs.org/joc Article

DFT Case Study of the Mechanism of a Metal-Free Oxygen Atom Insertion into a *p*-Quinone Methide C(sp^3)−C(sp^2) Bond

Ivor Smajlagic, Muhammad Kazim, Thomas Lectka,* and Travis Dudding*

Cite This: *J. Org. Chem.* 2020, 85, 10110−10117 Read Online

ACCESS | Metrics & More | Article Recommendations | Supporting Information

ABSTRACT: The site-selective introduction of an oxygen atom into an organic molecule, without the assistance of metals, is a useful transformation, though understanding the mechanistic underpinning of such a process is oftentimes a challenging task. In exploring this chemical space and in building upon experimental precedents, we have utilized computational tools to delineate the mechanistic details of site-selective oxygen atom insertion into a *p*-quinone methide C(sp^3)−C(sp^2) bond. To this end, several different reaction pathways for oxygen atom insertion were explored—each encompassing a unique element qualifying the respective pathway as being more or less feasible. The findings of these investigations revealed several features that were vital to this reactivity, including the formation of a dimeric intermediate, interconversion between ground- and excited-state species, and strain. Notably, the latter finding adds to the portfolio of strain-release-driven reactions that have emerged as popular methods to achieve otherwise difficult chemical transformations.

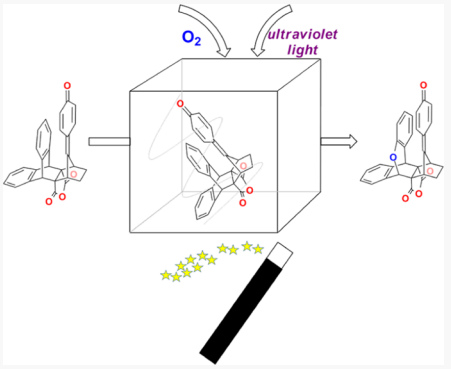

INTRODUCTION

Oxygen atom insertion is a fundamental transformation in both biological and chemical settings, as often called upon in the construction of ethers, esters, and alcohols from ubiquitous C−H and C−C bonds. From a biological standpoint, the cytochrome P450 enzymes are well known for their ability to facilitate oxygen atom insertion events providing bioactive compounds and related natural products, though the mechanism of these processes is an often debated topic.[1]

The venerable Baeyer−Villiger reaction, in contrast, is a commonly employed synthetic strategy for preparing esters and lactones from carbonyl-containing substrates.[2] In large part, the widespread use of this reaction derives from an understanding of the mechanism, thus demonstrating how with mechanistic insights, utility and experimental implementation follow. The mechanistic details of this reaction—involving the nucleophilic attack of peroxide at an electrophilic acyl carbon—whereupon alkyl (or aryl) migration follows with concomitant scission of the weak O−O peroxy bond furnishes RCO_2R' functional group-containing products. Notwithstanding, an inherent feature of this reactivity is the presence of a carbonyl group fulfilling the important role of directing C−C bond activation for oxygen atom insertion, in addition to the migratory aptitude of groups and stereoelectronic effects[3] (Figure 1A).

Alternatively, oxygen atom insertion into intrinsically inert C−C bonds, for example, C(sp^3)−C(sp^2) bonds, is a more formidable challenge, especially when attempting to enable site selectivity. This is especially true if dioxygen is the source of oxygen, despite its abundance. Nevertheless, this type of reactivity holds great potential, for example, in photodynamic therapies and recycling and synthesis as a powerful strategy for the rapid construction of molecular complexity utilizing readily available oxygen.[4] The key to unlocking this reactivity, arguably, is through mechanistic understanding, hand-in-hand with experimental investigations. In this regard, we recently reported the synthesis of a *p*-quinone methide (*p*-QM) (**1**, Figure 1B), which upon photolysis, in the presence of trace amounts of oxygen, underwent a highly selective oxygen insertion reaction at the proximate aromatic ring, as confirmed by ^{1}H and ^{13}C NMR and X-ray crystallography.[5] This type of reactivity is less commonly encountered and thus represents one among a very few instances of selective oxygen atom insertion into an intrinsically inert C(sp^3)−C(sp^2) chemical bond. On a related note, underscoring the emerging importance of oxygen atom insertion is a recent report by Aratani and Yamada groups, wherein direct oxygen atom insertion into a biaryl C(sp^2)−C(sp^2)σ-bond was achieved[6] (Figure 1B).

A common theme between both of these disclosures was alleviation of strain, for example, angle strain (Baeyer strain) and torsional strain (Pitzer strain), as intrinsic features for

Received: June 9, 2020
Published: July 7, 2020

https://dx.doi.org/10.1021/acs.joc.0c01371
J. Org. Chem. 2020, 85, 10110−10117

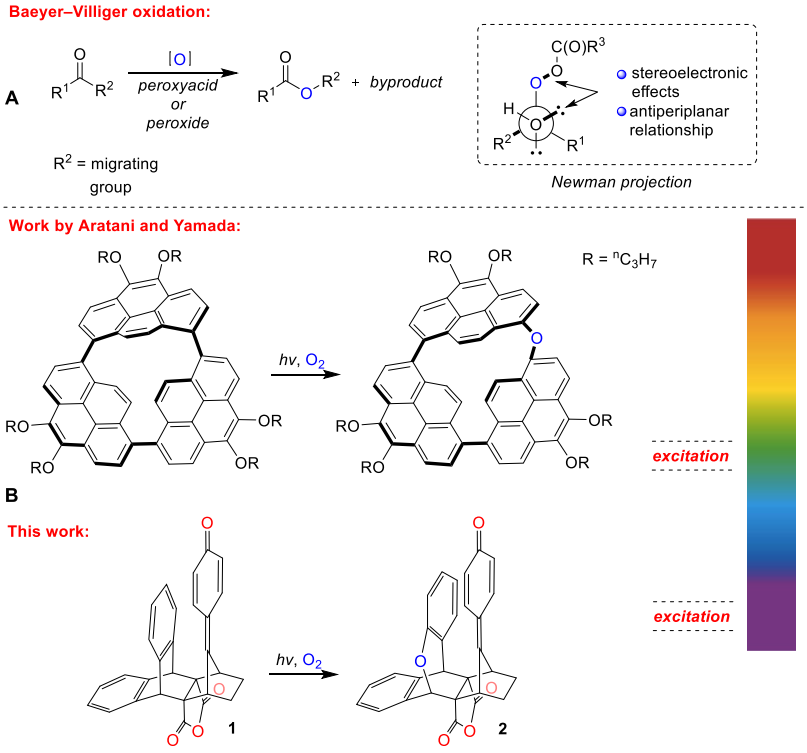

Figure 1. (A) General depiction of Baeyer–Villiger oxidation. (B) Existing strategies showcasing oxygen atom insertion into different bonds.

driving reactivity forward.[7] Incidentally, in terms of *p*-QM (**1**), we proposed a preliminary rationale for oxygen insertion; however, upon deeper consideration, it became evident that further investigation was required to explain the reactivity of this system. Toward this aim, there were a number of aspects needing to be addressed and/or further clarified, including (i) the role of solvent (acetonitrile), (ii) the absence of nitrile-derived byproducts, (iii) the possibility of H_2O-facilitated reaction pathway(s), and (iv) ultimately, a rigorous mechanistic investigation of different, presumably viable, modes of reactivity. Accordingly, herein, we describe a computational investigation exploring nonmetal-based oxygen atom insertion into $C(sp^3)-C(sp^2)$ bonds using a *p*-QM substrate (**1**) as an exemplar case. We posit that this disclosure will help evolve understanding of the mechanistic details inherent to photochemical processes.

RESULTS AND DISCUSSION

Strain and Photo-Induced Reactivity. Density functional theory (DFT) and time-dependent (TD)-DFT calculations at the [(IEFPCM)$_{(CH_3CN)}$]UB3LYP-D3/6-311++G(2d,2p)//UB3LYP/6-31G(d) level of theory were performed using the Gaussian 09 program[8−10] to gain an insight into the mechanism at hand (see the Supporting Information for details). Accordingly, with the aim of clarifying the basis of site-selective oxygen atom insertion into the $C(sp^3)-C(sp^2)$ bridgehead bond of *p*-QM (**1**), several underlying contributors came to the forefront (Figure 2). As a point of departure, we sought to gain an insight into the susceptibility of the bridgehead C−C bond, which was observed to undergo cleavage experimentally. In probing this aspect, using the X-ray crystal structure coordinates of *p*-QM (**1**) as input, in silico optimization provided computed *p*-QM with nearly identical

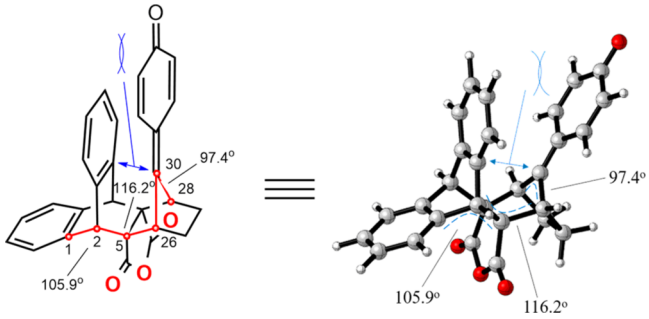

Figure 2. 2D (left-hand side) and 3D (right-hand side) structures of **1** with a few bond angles identified.

structural features, for example, bond distances, angles, and so forth.[5c]

Notably, the computed bond dissociation Gibbs free energy (BDFE) of the bridgehead bond of **1** equated to 61.4 kcal mol^{-1} (see the Supporting Information for details) well below typical C−C bond strengths, for example, Ph-Me with a BDFE of 102 kcal mol^{-1}.[11] The weakening of this bond, in part, derives from steric repulsion between the *p*-QM and proximal aryl bridgehead carbons, as conferred by short C···C distances of 2.99 Å, a metric well below the sum of the van der Waals radii of two carbons (Pauling van der Waal radius *C* = 1.70 Å).[12] Furthermore, there were various aberrant angles and torsions throughout the polycyclic framework resulting in Baeyer strain, for example, $\theta_{C(1)-C(2)-C(5)}$ = 105.9°, $\theta_{C(2)-C(5)-C(26)}$ = 116.2°, and $\theta_{C(26)-C(30)-C(28)}$ = 97.4°.

Associated with these elements of strain was the important role of the *p*-QM moiety in triggering reactivity, as clearly seen from the computed highest occupied molecular orbital (HOMO) and the lowest unoccupied molecular orbital

https://dx.doi.org/10.1021/acs.joc.0c01371
J. Org. Chem. 2020, 85, 10110−10117

(LUMO) of *p*-QM (**1**) with orbital densities completely localized on the quinone ring moiety (Figure 3).

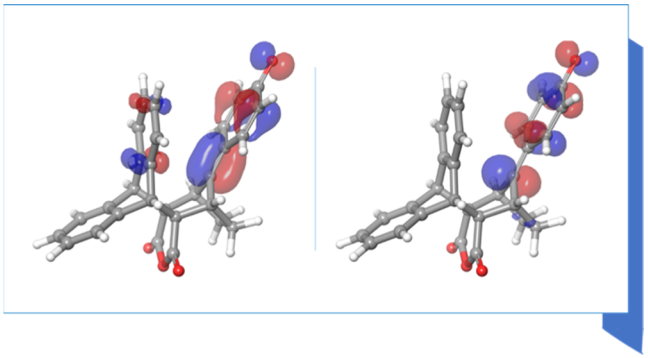

Figure 3. Computed [UB3LYP-D3/6-311++G (2d,2p)//UB3LYP/6-31G(d)] HOMO (left-hand side) and LUMO (right-hand side) of **1**.

Pathways 1−4. With a glimpse into the inherent strain and indispensable role of the *p*-QM moiety of **1**, our attention turned to examining several reaction scenarios deemed most probable. Collectively, these differing processes defined four pathways, all of which featured pivotal peroxy radical $\mathbf{5_{T1}}$ and/or benzyl diradical $\mathbf{4_{T1}}$ (Figures 4, 5, and 7, pathways 1−4).

A brief overview of computed pathways 1 and 2 reveals great differences between them until intermediate $\mathbf{5_{T1}}$, primarily the involvement of singlet vs. triplet dioxygen, wherein the two pathways converged after $\mathbf{5_{T1}}$ to provide product $\mathbf{3_{S1}}$. Markedly, only singlet-state species were involved in the steps preceding intermediate $\mathbf{5_{T1}}$ in pathway 1 (blue line), whereas pathway 2 proceeded through intersystem crossing (ISC) following photolysis, wherein a rearrangement of the bicyclo[2.2.2]-framework of **1** occurred. Here, two distinct steps were found to exist with the intermediates being triplet-state species (pathway 2, red line) (Figure 4).

Taking a finer look at the mechanistic details of pathway 1, an excited-state intermediate $\mathbf{1S_1^*}$, residing at 45.0 kcal mol^{-1} above the ground-state-starting structure $\mathbf{1S_1}$ on the reaction coordinate diagram, initially forms following the absorption of a photon of light. Either internal conversion back to the ground state or forward propagation along the reaction pathway then occurs with the latter involving funneling through a conical intersection emptying onto the ground-state surface at intermediate $\mathbf{2_{S1}}$ via transition state $\mathbf{TS1_{S1}}$, displaying C···C bond-making and bond-breaking distances of 1.66 and 2.21 Å, respectively (Figure 4). Singlet-state intermediate $\mathbf{2_{S1}}$ next reacts with triplet dioxygen to furnish the intermediate $\mathbf{5_{T1}}$, with its spin density localized on the quinone ring and the peroxy radical group, clearly foreshadowing the subsequent reactivity (Figure 6). With the stage set, the peroxy radical oxygen addition to the abundant solvent occurs by the energetically demanding transition state $\mathbf{TS3_{T1}}$ (calculated $\Delta G^{\ddagger}$ = 28.3 kcal mol^{-1}) featuring a C···O bond-forming distance of 1.75 Å. This endergonic process leads to iminyl radical $\mathbf{6_{T1}}$, wherein the spin is dispersed across the quinone ring and the peroxy iminyl substructure. The subsequent O−O bond homolysis (transition state $\mathbf{TS4_{T1}}$) with a O···O bond-breaking distance of 2.10 Å and a moderate Gibbs free energy activation barrier ($\Delta G^{\ddagger}$) of 15.5 kcal mol^{-1} is then surmounted to provide triplet-state intermediate $\mathbf{7_{T1}}$, concomitant with a putative nitrile-derived oxaziridine-like byproduct. Thereafter, attack of the oxygen-centered radical of $\mathbf{7_{T1}}$ upon the neighboring aromatic ring ensues to form

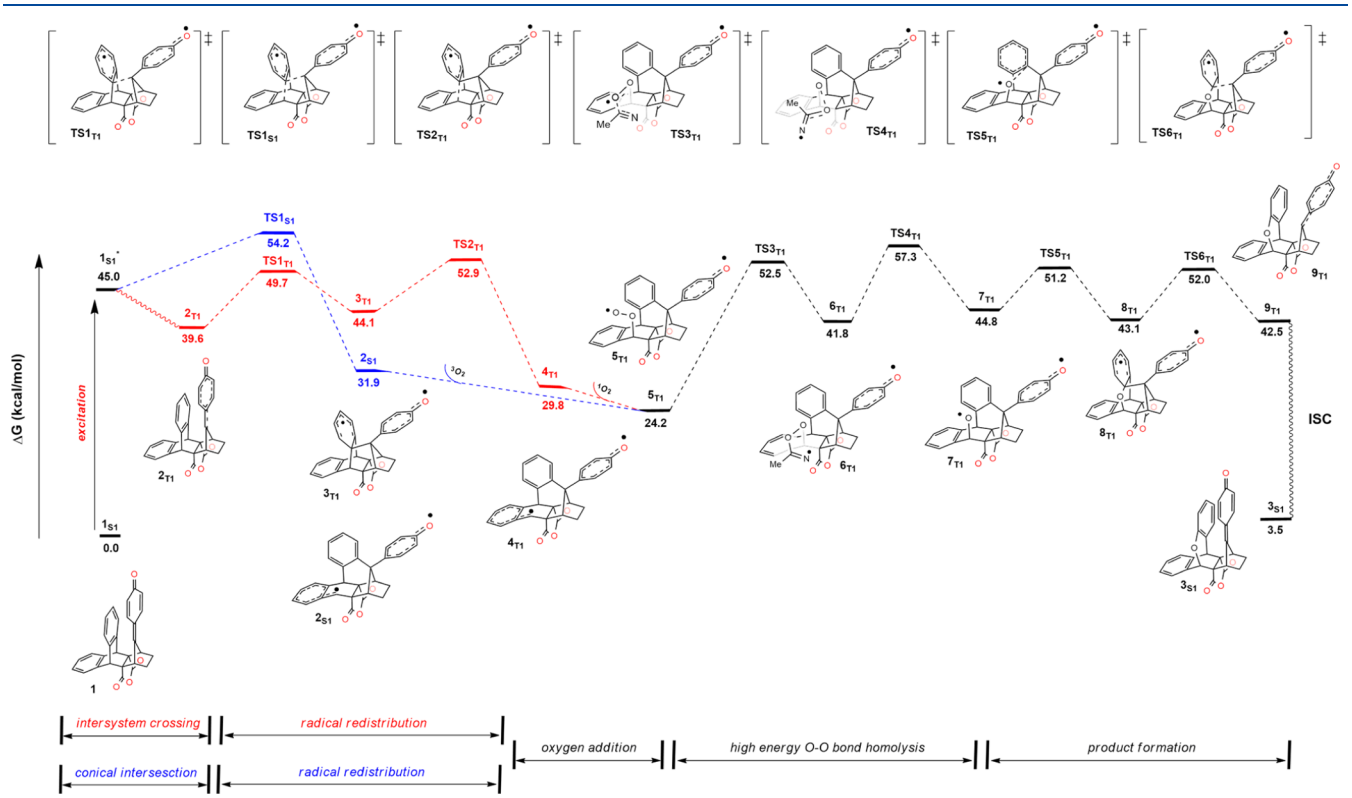

Figure 4. Comparative free energy profiles for oxygen atom insertion via pathways 1 (blue) and 2 (red). These profiles share a common pathway upon formation of intermediate $\mathbf{5_{T1}}$.

https://dx.doi.org/10.1021/acs.joc.0c01371
J. Org. Chem. 2020, 85, 10110−10117

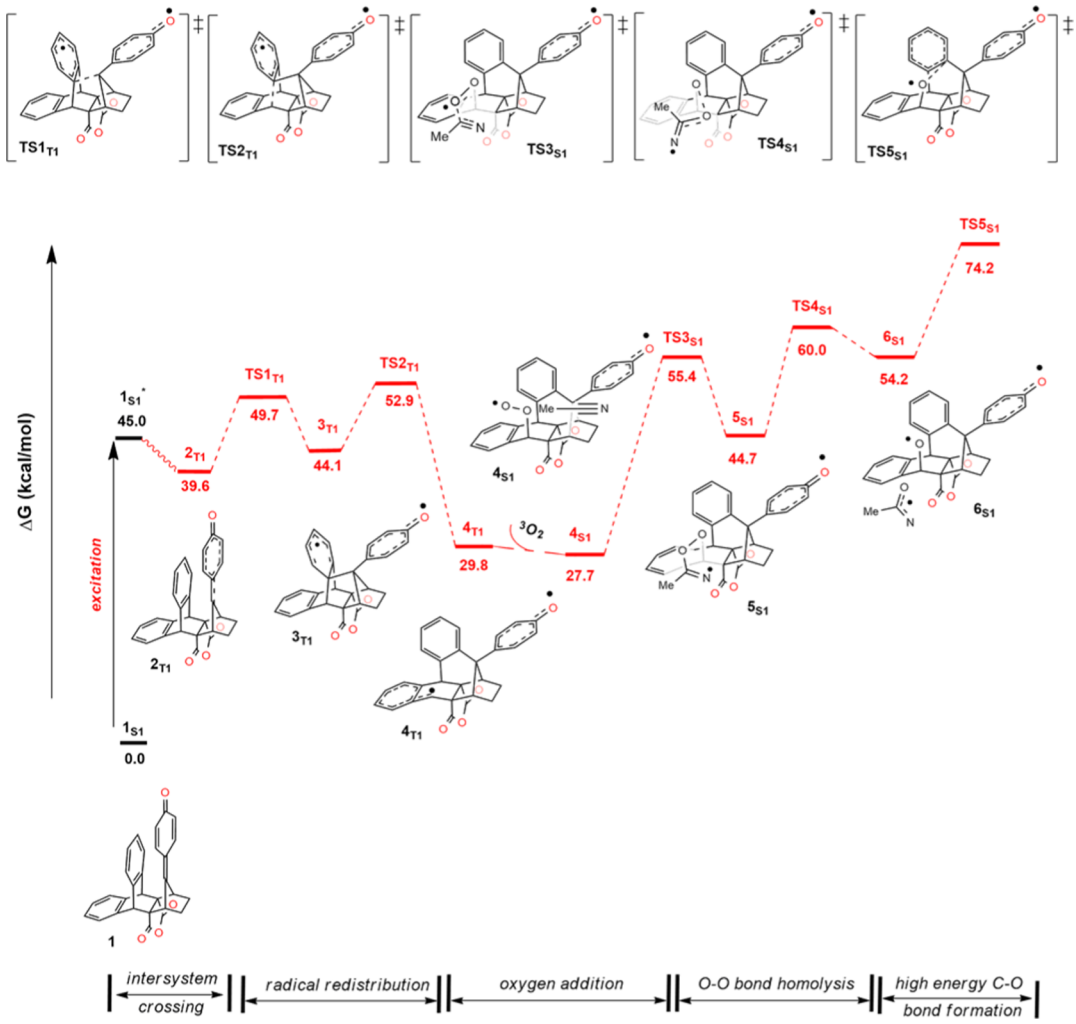

Figure 5. Free energy profile for oxygen atom insertion via pathway 3. This reaction pathway was truncated at high-energy transition state $\mathbf{TS5}_{S1}$.

resonance-stabilized aryl radical $\mathbf{8}_{T1}$ by C···O bond-forming (distance = 1.91 Å) transition state $\mathbf{TS5}_{T1}$ with a calculated activation barrier of 6.40 kcal mol^{-1}. At that stage, C−C bond homolysis by $\mathbf{TS6}_{T1}$, displaying a C···C bond-breaking distance of 2.17 Å and a calculated activation barrier of 8.90 kcal mol^{-1}, forms triplet-state intermediate $\mathbf{9}_{T1}$. Finally, relaxation to the ground state affords computed singlet-state product $\mathbf{3}_{S1}$ corresponding to product **2**.

As for pathway 2, initial ISC from $\mathbf{1S}_1^*$ furnishes triplet-state intermediate $\mathbf{2}_{T1}$, which is 39.6 kcal mol^{-1} less stable than the starting *p*-QM (**1**) and dominated by the QM ring-localized spin density (Figures 4 and 6). Quinone methide and proximal aryl ring C−C bond formation (distance = 2.12 Å) coupled to the migration of quinone ring spin density onto the neighboring aryl ring then occurs by transition state $\mathbf{TS1}_{T1}$ with an activation energy of 10.1 kcal mol^{-1}. The resulting resonance-stabilized aryl radical $\mathbf{3}_{T1}$ then undergoes C−C bond scission (distance = 2.07 Å) by transition state $\mathbf{TS2}_{T1}$ with an activation barrier of 8.80 kcal mol^{-1} to furnish benzyl diradical $\mathbf{4}_{T1}$, wherein the spin density is localized on the quinone ring and benzylic carbon (Figure 6). At that point, reaction with singlet dioxygen, presumably generated by oxygen quenching of $\mathbf{1}_{S1}^*$ with *p*-QM (**1**) playing the role of a sensitizer and light,[13] affords peroxy radical $\mathbf{5}_{T1}$. Thereafter, and as noted above, the remaining steps of this pathway mirror those of pathway 1.

In stepping back and generalizing the overall feasibility of these two pathways, both are fraught with the unfavorable energetics of proceeding through transition state $\mathbf{TS3}_{T1}$—that is, capture of the solvent—provided the viability of the ISC or the event of a conical intersection. Taking this into consideration, these two pathways, nonetheless, offer a more probable mechanism for the formation of $\mathbf{3}_{S1}$ from $\mathbf{1}_{S1}$ than the highly unfavorable peroxy radical addition to the solvent (singlet state) nitrile nitrogen[5c] $\mathbf{S6}_{T1}$ (calculated $\Delta G^{\ddagger}$ = 53.9 kcal mol^{-1}) (see the Supporting Information).

Pathway 3, as a less viable option, is built upon the elements of pathways 1 and 2, wherein the common denominator appears to be intermediate $\mathbf{4}_{T1}$ that utilizes triplet-state oxygen to provide marginally more stable intermediate $\mathbf{4}_{S1}$ (Figure 5). This singlet-state intermediate then reacts with the solvent by energetically demanding transition state $\mathbf{TS3}_{S1}$, which is 27.7 kcal mol^{-1} less stable than intermediate $\mathbf{4}_{S1}$. The product of solvent capture (intermediate $\mathbf{5}_{S1}$) then undergoes O−O bond homolysis (distance = 1.97 Å) by transition state $\mathbf{TS4}_{S1}$ affording oxygen-centered radical $\mathbf{6}_{S1}$. At that point, oxygen addition to the nearby aryl ring was computed to be highly unfavorable with an activation barrier of 20.0 kcal mol^{-1} for surmounting transition state $\mathbf{TS5}_{S1}$, located well above $\mathbf{1}_{S1}$ or,

https://dx.doi.org/10.1021/acs.joc.0c01371
J. Org. Chem. 2020, 85, 10110−10117

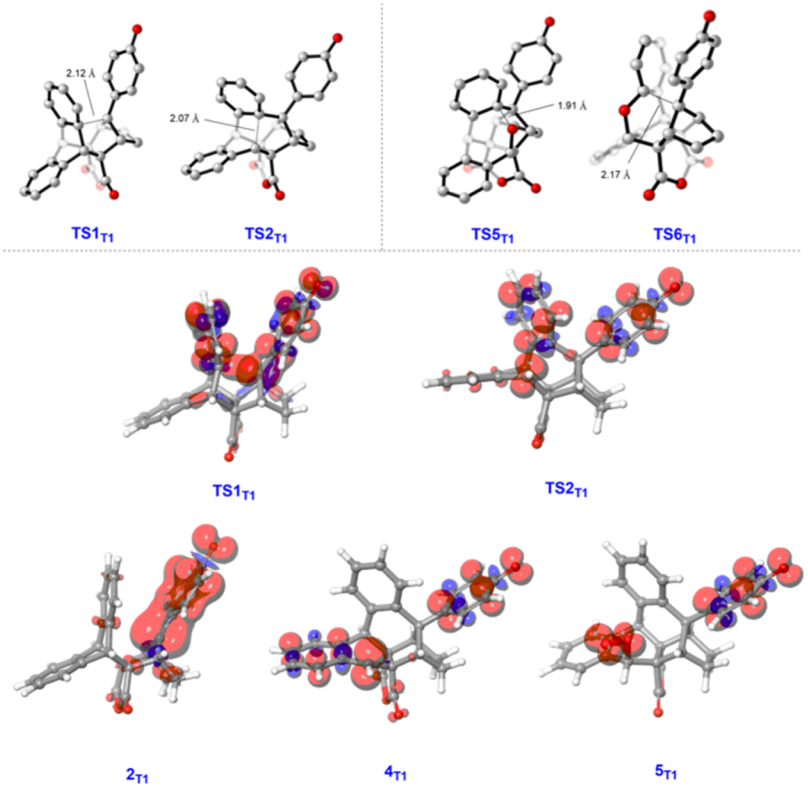

Figure 6. Calculated geometries of transition-state structures (triplet state) with key bond metrics shown in Å, along with spin densities of prominent transition states and intermediates.

for that matter, $\mathbf{1}^{*}_{S1}$. Given this escalating energetic profile and, with it, infeasibility of this mechanistic scenario, further investigation of this pathway was not pursued. Finally, having ruled out this pathway as a possibility, we explored one final option, namely, pathway 4.

Pathway 4, in reserving the principle elements of pathway 2, affords $\mathbf{3}_{S1}$ from $\mathbf{1}_{S1}$ by a series of energetically favorable steps, making this pathway the most feasible one among the investigated pathways (Figure 7). The finer details of pathway 4 similarly evolve until triplet state peroxy radical $\mathbf{5}_{T1}$. At that juncture, peroxy radical $\mathbf{5}_{T1}$ combines with benzyl diradical $\mathbf{4}_{T1}$, despite a slight entropic penalty, to provide a more stable dimer intermediate (7_{S1}) located at 8.5 kcal mol^{-1} below triplet-state precursor $\mathbf{5}_{T1}$ on the reaction coordinate by a process ($\mathbf{ETS}_{T1}$) with an estimated activation barrier of 14.0 kcal mol^{-1}, as determined from BDFE values. Dimer break-up affording 7_{T1} from 7^{*}_{S1} by a well-defined first-order saddle point was also investigated; however, this enterprise proved intractable and, with it, the assumption that light-mediated O−O bond homolysis[14,15] has sufficiently large energy to make propagation of oxygen-centered radical 7_{T1} toward the product favorable, as opposed to its recombination back to 7_{S1}. Alternatively, one could invoke the formation of a putative dimer with a tetraoxygen functionality acting as a bridging element. Notwithstanding, the energy of this process was prohibitively high ($\mathbf{S8}_{S1}$) at 79.2 kcal mol^{-1} (see the Supporting Information), thus ruling out this possibility. Irrespectively, from 7_{T1}, transition state $\mathbf{TS5}_{T1}$ emerges with an activation barrier of 6.40 kcal mol^{-1} and a C···O bond-forming distance of 1.91 Å. The resulting resonance-stabilized aryl radical $\mathbf{8}_{T1}$ then undergoes C−C bond homolysis via transition state $\mathbf{TS6}_{T1}$ having a C···C bond-breaking distance of 2.17 Å and a computed activation barrier of 8.90 kcal mol^{-1} leading to triplet-state intermediate $\mathbf{9}_{T1}$. Finally, relaxation to the ground state affords computed singlet state $\mathbf{3}_{S1}$ corresponding to product **2**.

Synopses. In reflecting upon the above mechanistic possibilities, proposed pathway 4 stands out as the most viable option. Governing this preference are strain, photo-responsive functionality (QM moiety), and spin and/or charge delocalization within *p*-QM (**1**). Nonetheless, the insights from this model system, arguably, provide a compelling case of nonmetal-mediated oxygen atom insertion benefiting from abundant molecular oxygen as the terminal oxidant and light.

Further to this point, the experimental observations realized in our previous report[5c] are concordant with the computational findings associated with pathway 4, namely, solvent- and H_2O-related implications. Experimentally, nitrile solvents were found to be an integral component for reactivity, which was previously an open-ended question that we now attribute to charge stabilization and/or quinone carbonyl polarization triggering photolysis-driven bond breaking and sensitization—among other events. This plausible indirect involvement of solvent in the mechanism also sheds light on the questions raised relating to the observed absence of nitrile-derived byproducts. Last, the possibility of obtaining hydrated side products can be accounted for by either reaction of the peroxide group present in the dimer with H_2O or a possible change in the mechanism (ionic vs radical) that would be influenced by a change in the chemical environment, that is, H_2O-induced (see the Supporting Information for details).

https://dx.doi.org/10.1021/acs.joc.0c01371
J. Org. Chem. 2020, 85, 10110−10117

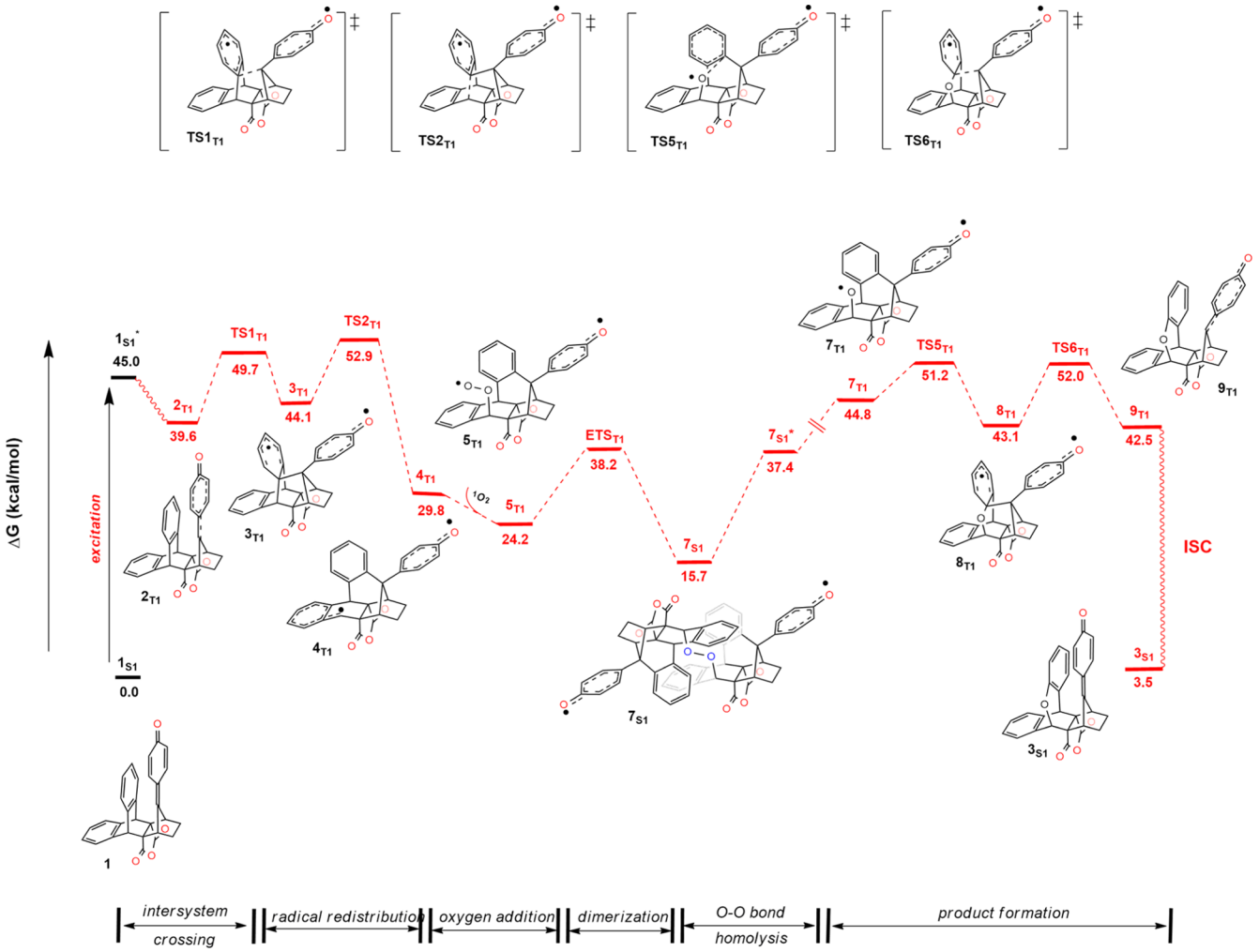

Figure 7. Free energy profile for oxygen atom insertion via pathway 4. This pathway involves dimer species $\mathbf{7_{S1}}$ as a pivotal intermediate deemed necessary to access the product.

CONCLUSIONS

In this article, additional insights regarding the mechanism of oxygen atom insertion into an aromatic *p*-QM C(sp^3)−C(sp^2) bond of **1** were provided. Employing DFT calculations, a feasible pathway, among others investigated, was uncovered that hinged upon the formation of a key dimeric intermediate. Furthermore, this pathway revealed a mechanistic scenario that supported the absence of nitrile-derived byproducts while providing viable reasoning for the formation of hydrated side products in the presence of H_2O, thus supporting empirical findings. Salient to this reactivity were the roles of earth-abundant molecular oxygen as an oxidant and light as a driving force. As this type of reactivity is still in its infancy, it is projected that the results of this study will serve as an instructive conceptual resource for emerging studies exploring nonmetal-based oxygen atom insertion processes.

EXPERIMENTAL SECTION

Computational Details. DFT calculations were performed using the software package Gaussian 09, Revision E. 01.[8] All optimizations were performed applying the B3LYP functional (unrestricted) that includes Becke's three-parameter gradient-corrected exchange functional[16] and the LYP correlation functional[17] of Lee, Yang, and Parr along with the 6-31G(d) basis set. The optimized geometries were verified as transition-state structures (one imaginary frequency) or minima (zero imaginary frequencies) by frequency calculations. Intrinsic reaction coordinate calculations[18,19] were performed to confirm that all transition-state structures were linked to relevant minima. The energies of the UB3LYP/6-31G(d) optimized structures were further refined by single-point calculations performed at the UB3LYP-D3/6-311++G(2d,2p) level of theory using the integral equation formalism polarizable continuum model (IEFPCM) with the default parameters of acetonitrile (ε = 37.5) to account for solvent[20] and dispersion accounted for by the Grimme[21] dispersion correction method. The final reported Gibbs free energies are the summed thermal corrections to the Gibbs free energies (temperature = 298.15 K) computed at the lower [UB3LYP/6-31G(d)] level of theory and electronic energies from single-point UB3LYP-D3/6-311++G(2d,2p) calculations. Single-point TD-DFT calculations were computed at the TD−SCF−IEFPCM($_{CH3CN}$)UB3LYP-D3/6-311++G(2d,2p) level of theory using the UB3LYP/6-31G(d) optimized geometries. The keyword (integral = grid = ultrafine) was used for all calculations. Stable calculations were performed to verify that the computed wavefunctions of each of the calculated structures were stable. Moreover, any structure with an internal wavefunction instability was reoptimized using stable/broken-symmetry calculations at the IEFPCM($_{CH3CN}$)UB3LYP-D3/6-311++G(2d,2p) level of theory; however, structurally large $\mathbf{S8_{S1}}$ was not reoptimized owing to computational limitations. These energies and thermal corrections (UB3LYP/6-31G(d)—same as above) were then summed to provide the final reported Gibbs free energies. The 3D images of all optimized geometries were generated with CYLview,[22] and GaussView[10] was used to construct all structures prior to optimization and to visualize

https://dx.doi.org/10.1021/acs.joc.0c01371
J. Org. Chem. 2020, 85, 10110−10117

the output from the Gaussian 09 calculations. The reported spin orbital densities (isovalue = −0.0045) and HOMO and LUMO molecular orbitals (isovalue = −0.05) were calculated using the UB3LYP-D3 functional with a 6-311++G(2d,2p) basis set using the program Jaguar of the Schrödinger software package.[23]

■ ASSOCIATED CONTENT

Supporting Information

The Supporting Information is available free of charge at https://pubs.acs.org/doi/10.1021/acs.joc.0c01371.

Computational calculations and their corresponding data; optimized structures of acetonitrile, nitrile by-product, and singlet and triplet oxygen, transition state and intermediate state; and schematics of photo-hydration and oxygen atom insertion (PDF)

■ AUTHOR INFORMATION

Corresponding Authors

Thomas Lectka − *Department of Chemistry, Johns Hopkins University, Baltimore, Maryland 21218, United States;* orcid.org/0000-0003-3088-6714; Email: lectka@jhu.edu

Travis Dudding − *Department of Chemistry, Brock University, St. Catharines, Ontario L2S 3A1, Canada;* orcid.org/0000-0002-2239-0818; Email: tdudding@brocku.ca

Authors

Ivor Smajlagic − *Department of Chemistry, Brock University, St. Catharines, Ontario L2S 3A1, Canada*

Muhammad Kazim − *Department of Chemistry, Johns Hopkins University, Baltimore, Maryland 21218, United States*

Complete contact information is available at: https://pubs.acs.org/10.1021/acs.joc.0c01371

Notes

The authors declare no competing financial interest.

■ ACKNOWLEDGMENTS

T.D. acknowledges financial support from the Natural Science and Engineering Research Council (NSERC) Discovery Grant (2019-04205). I.S. acknowledges QEII-GSST for funding. Computations were carried out using facilities at SHARCNET (Shared Hierarchical Academic Research Computing Network: www.sharcnet.ca) and Compute/Calcul Canada. T.L. thanks the National Science Foundation (NSF) (grant CHE 1800510) for financial support. We also thank Scheherzad Alvi from the Singleton Group for constructive and helpful discussions.

■ REFERENCES

(1) Hamdane, D.; Zhang, H.; Hollenberg, P. Oxygen Activation by Cytochrome P450 Monooxygenase. *Photosynth. Res.* **2008**, *98*, 657−666.

(2) (a) Baeyer, A.; Villiger, V. On the Reactivity of Caro's Reagents with Ketones. *Ber. Dtsch. Chem. Ges.* **1900**, *33*, 858−864. (b) Baeyer, A.; Villiger, V. Reactivity of Caro's Reagents with Ketones. *Ber. Dtsch. Chem. Ges.* **1899**, *32*, 3625−3633.

(3) ten Brink, G.-J.; Arends, I. W. C. E.; Sheldon, R. A. The Baeyer−Villiger Reaction: New Developments toward Greener Procedures. *Chem. Rev.* **2004**, *104*, 4105−4124.

(4) (a) Frahm, M.; Drathen, T.; Gronbach, L. M.; Voss, A.; Lorenz, F.; Bresien, J.; Villinger, A.; Hoffmann, F.; Brasholz, M. Visible-Light Cascade Photooxygenation of Tetrahydrocarbazoles and Cyclohepta-[b]indoles: Access to C,N-Diacyliminium Ions. *Angew. Chem., Int. Ed.* **2020**, *59*, 12450−12454. (b) Klaper, M.; Linker, T. Intramolecular Transfer of Singlet Oxygen. *J. Am. Chem. Soc.* **2015**, *137*, 13744−13747. (c) Lucky, S. S.; Soo, K. C.; Zhang, Y. Nanoparticles in Photodynamic Therapy. *Chem. Rev.* **2015**, *115*, 1990−2042. (d) Wencel-Delord, J.; Dröge, T.; Liu, F.; Glorius, F. Towards Mild Metal-Catalyzed C−H Bond Activation. *Chem. Soc. Rev.* **2011**, *40*, 4740−4761. (e) Wendlandt, A. E.; Suess, A. M.; Stahl, S. S. Copper-Catalyzed Aerobic Oxidative C−H Functionalizations: Trends and Mechanistic Insights. *Angew. Chem., Int. Ed.* **2011**, *50*, 11062−11087. (f) Montagnon, T.; Noutsias, D.; Alexopoulou, I.; Tofi, M.; Vassilikogiannakis, G. Green Oxidations of Furans−Initiated by Molecular Oxygen−that give key natural product motifs. *Org. Biomol. Chem.* **2011**, *9*, 2031−2039. (g) Montagnon, T.; Tofi, M.; Vassilikogiannakis, G. Using Singlet Oxygen to Synthesize Polyoxygenated Natural Products from Furans. *Acc. Chem. Res.* **2008**, *41*, 1001−1011. (h) Chin, K. K.; Trevithick-Sutton, C. C.; McCallum, J.; Jockusch, S.; Turro, N. J.; Scaiano, J. C.; Foote, C. S.; Garcia-Garibay, M. A. Quantitative Determination of Singlet Oxygen Generated by Excited State Aromatic Amino Acids, Proteins, and Immunoglobulins. *J. Am. Chem. Soc.* **2008**, *130*, 6912−6913. (i) Tromberg, B. J.; Kimel, S.; Orenstein, A.; Barker, S. J.; Hyatt, J.; Nelson, J. S.; Roberts, W. G.; Berns, M. W. Tumor Oxygen Tension During Photodynamic Therapy. *J. Photochem. Photobiol., B* **1990**, *5*, 121−126.

(5) (a) Kazim, M.; Siegler, M. A.; Lectka, T. A Case of Serendipity: Synthesis, Characterization, and Unique Chemistry of a Stable, Ring Unsubstituted Aliphatic p-Quinone Methide. *Org. Lett.* **2019**, *21*, 2326−2329. (b) Kazim, M.; Siegler, M. A.; Lectka, T. A Protonated Quinone Methide Stabilized by a Combination of Partial Aromatization and π-Interaction: Spectroscopic and Crystallographic Analysis. *J. Org. Chem.* **2019**, *84*, 8284−8288. (c) Kazim, M.; Foy, H.; Siegler, M. A.; Dudding, T.; Lectka, T. Discovery and Mechanistic Study of a Totally Organic $C_{(aryl)}$−$C_{(alkyl)}$Oxygen Insertion Reaction. *J. Org. Chem.* **2019**, *84*, 14349−14353.

(6) Kurosaki, R.; Hayashi, H.; Suzuki, M.; Jiang, J.; Hatanaka, M.; Aratani, N.; Yamada, H. A Remarkably Strained Cyclopyrenylene Trimer that Undergoes Metal-Free Direct Oxygen Insertion into the Biaryl C−C σ-Bond. *Chem. Sci.* **2019**, *10*, 6785−6790.

(7) Anslyn, E. V.; Dougherty, D. A. *Modern Physical Organic Chemistry*; University Science Books: Sausalito, 2006.

(8) Frisch, M. J.; Trucks, G. W.; Schlegel, H. B.; Scuseria, G. E.; Robb, M. A.; Cheeseman, J. R.; Scalmani, G.; Barone, V.; Mennucci, B.; Petersson, G. A.; Nakatsuji, H.; Caricato, M.; Li, X.; Hratchian, H. P.; Izmaylov, A. F.; Bloino, J.; Zhang, G.; Sonnenberg, J. L.; Hada, M.; Ehara, M.; Toyota, K.; Fukuda, R.; Hasegawa, J.; Ishida, M.; Nakajima, T.; Honda, Y.; Kitao, O.; Nakai, H.; Vreven, T.; Montgomery, J. A., Jr.; Peralta, J. E.; Ogliaro, F.; Bearpark, M.; Heyd, J. J.; Brothers, E.; Kudin, K. N.; Staroverov, V. N.; Kobayashi, R.; Normand, J.; Raghavachari, K.; Rendell, A.; Burant, J. C.; Iyengar, S. S.; Tomasi, J.; Cossi, M.; Rega, N.; Millam, J. M.; Klene, M.; Knox, J.; Cross, J. B.; Bakken, V.; Adamo, C.; Jaramillo, J.; Gomperts, R.; Stratmann, R. E.; Yazyev, O.; Austin, A. J.; Cammi, A. R.; Pomelli, C.; Ochterski, J. W.; Martin, R. L.; Morokuma, K.; Zakrzewski, V. G.; Voth, G. A.; Salvador, P.; Dannenberg, J. J.; Dapprich, S.; Daniels, A. D.; Farkas, O.; Foresman, J. B.; Ortiz, J. V.; Cioslowski, J.; Fox, D. J. *Gaussian 09*, Revision E.01; Gaussian, Inc.: Wallingford, CT, 2009.

(9) Chai, J.-D.; Head-Gordon, M. Long-Range Corrected Hybrid Density Functionals with Damped Atom−Atom Dispersion Corrections. *Phys. Chem. Chem. Phys.* **2008**, *10*, 6615−6620.

(10) Dennington, R.; Keith, T.; Millam, J. *GaussView*, version 5; Semichem, Inc.: Shawnee Mission, 2009.

(11) Pedley, J. B.; Naylor, R. D.; Kirby, S. P. *Thermochemical Data of Organic Compounds*, 2nd ed.; Chapman and Hall: New York, 1986.

(12) Batsanov, S. S. Van der Waals Radii of Elements. *Inorg. Mater.* **2001**, *37*, 871−885.

(13) (a) Ge, J.; Lan, M.; Zhou, B.; Liu, W.; Guo, L.; Wang, H.; Jia, Q.; Niu, G.; Huang, X.; Zhou, H.; Meng, X.; Wang, P.; Lee, C.-S.; Zhang, W.; Han, X. A Graphene Quantum Dot Photodynamic Therapy Agent with High Singlet Oxygen Generation. *Nat. Commun.* **2014**, *5*, 4596−4604. (b) Dolmans, D. E. J. G. J.; Fukumura, D.; Jain,

R. K. Photodynamic Therapy for Cancer. *Nat. Rev. Cancer* **2003**, *3*, 380−387.
(14) Abel, B.; Assmann, J.; Botschwina, P.; Buback, M.; Kling, M.; Oswald, R.; Schmatz, S.; Schroeder, J.; Witte, T. Experimental and Theoretical Investigations of the Ultrafast Photoinduced Decomposition of Organic Peroxides in Solution: Formation and Decarboxylation of Benzoyloxy Radicals. *J. Phys. Chem. A* **2003**, *107*, 5157−5167.
(15) Yaremenko, I. A.; Vil', V. A.; Demchuk, D. V.; Terent'ev, A. O. Rearrangements of Organic Peroxides and Related Processes. *Beilstein J. Org. Chem.* **2016**, *12*, 1647−1748.
(16) Becke, A. D. Density-functional Thermochemistry. III. The Role of Exact Exchange. *J. Chem. Phys.* **1993**, *98*, 5648−5652.
(17) Lee, C.; Yang, W.; Parr, R. G. Development of the Colle-Salvetti Correlation-energy Formula into a Functional of the Electron Density. *Phys. Rev. B* **1988**, *37*, 785−789.
(18) González, C.; Schlegel, H. B. Reaction path following in mass-weighted internal coordinates. *J. Phys. Chem.* **1990**, *94*, 5523−5527.
(19) Fukui, K. The Path of Chemical Reactions − The IRC Approach. *Acc. Chem. Res.* **1981**, *14*, 363−368.
(20) Cancès, E.; Mennucci, B.; Tomasi, J. A New Integral Equation Formalism for the Polarizable Continuum Model: Theoretical Background and Applications to Isotropic and Anisotropic Dielectrics. *J. Chem. Phys.* **1997**, *107*, 3032−3041.
(21) Grimme, S. Semiempirical GGA-Type Density Functional Constructed with a Long-Range Dispersion Correction. *J. Comput. Chem.* **2006**, *27*, 1787−1799.
(22) Legault, C. Y. *CYLview*, version 1.0b; Universite de Sherbrooke: Quebec, Canada, 2009, http://www.cylview.org.
(23) *Schrödinger Release 2019−2: Jaguar*; Schrödinger, LLC: New York, 2019.

https://dx.doi.org/10.1021/acs.joc.0c01371
J. Org. Chem. 2020, 85, 10110−10117